



# Modeling of cold start processes and performance optimization for proton exchange membrane fuel cell stacks



Yibo Zhou, Yueqi Luo, Shuhai Yu, Kui Jiao\*

State Key Laboratory of Engines, Tianjin University, 92 Weijin Rd, Tianjin 300072, China

## HIGHLIGHTS

- A PEMFC cold start stack model is developed.
- A novel variable heating and load control (VHLC) method is proposed.
- Dead individual cells can be activated again by other cells with VHLC.
- Proper VHLC improves cold start performance significantly.

## ARTICLE INFO

### Article history:

Received 15 March 2013

Received in revised form

16 August 2013

Accepted 6 September 2013

Available online 17 September 2013

### Keywords:

Proton exchange membrane fuel cell (PEMFC)

Stack

Cold start

Model

Variable heating and load control (VHLC)

## ABSTRACT

In this study, a cold start model for proton exchange membrane fuel cell (PEMFC) stacks is developed, and a novel start-up method, variable heating and load control (VHLC), is proposed and evaluated. The main idea is to only apply load to the neighboring still-active cells, and to apply external heating to certain cells inside the stack simultaneously (load is not applied to the cells fully blocked by ice, although these cells can gain heat from neighboring cells). With the VHLC method, it is found that the stack voltage first increases, then decreases due to the full blockage of ice in some of the individual cells, and finally the dead cells are heated by the other active cells and activated again one by one. Based on this method, the external heating power and the stack self-heating ability are utilized more efficiently. With proper implementation of the VHLC method, it is demonstrated that the cold start performance can be improved significantly, which is critically important for PEMFC in automotive applications.

© 2013 Elsevier B.V. All rights reserved.

## 1. Introduction

Although proton exchange membrane fuel cell (PEMFC) is considered as one of the most suitable energy conservation devices in the future for automotive applications, there are still some technical issues to be solved before its commercial application. Among the different technical issues, start-up from subzero temperatures, known as “cold start”, is an important one, because the ice formed during the cold start processes can block the reaction sites, hindering the reactant transport and causing material degradation.

Most of the previous experimental studies of PEMFC cold start were conducted for performance degradation measurement [1–6], ice formation visualization [7–9] and property characterization

[10–15]. On the other hand, mathematical models are needed to study the detailed transport processes. One-dimensional models and analytical models were first developed to study the variations of voltage, current and temperature during the cold start processes [16–18]. Sundaresan and Moore [19] developed a one-dimensional thermal model for simulating the cold start processes of PEMFC stack, and this model separated the fuel cell into different layers to obtain the one-dimensional temperature distribution in a stack. Another one-dimensional cold start model for PEMFC stack was developed by Khandelwal et al. [20] to investigate the effects of various operating conditions and external heating methods on the start-up performance. Moreover, more detailed transport phenomena during the cold start processes of PEMFC were investigated based on multi-dimensional multiphase models in recent years [21–28]. For example, Jiao and Li [25,26] developed a three-dimensional multiphase model to simulate the cold start processes in a single PEMFC with straight flow channels, and investigated the various transport characteristics. Guo et al. [27]

\* Corresponding author. Tel.: +86 22 27404460; fax: +86 22 87401979.  
E-mail address: [kjiao@tju.edu.cn](mailto:kjiao@tju.edu.cn) (K. Jiao).

**Nomenclature**

$A$	cell geometric area, $\text{m}^2$
$ASR$	area specific resistance, $\Omega \text{ m}^2$
$c$	mole concentration, $\text{mol m}^{-3}$
$C_p$	specific heat, $\text{J kg}^{-1} \text{ K}^{-1}$
$D$	mass diffusivity, $\text{m}^2 \text{ s}^{-1}$
$EW$	equivalent weight of membrane, $\text{kg kmol}^{-1}$
$F$	Faraday's constant, $96487 \text{ C mol}^{-1}$
$h$	surrounding heat transfer coefficient, $\text{W m}^{-2} \text{ K}^{-1}$
$I$	current density, $\text{A cm}^{-2}$
$j$	reaction rate, $\text{A m}^{-3}$
$k$	thermal conductivity, $\text{W m}^{-1} \text{ K}^{-1}$
$M$	molecular weight, $\text{kg mol}^{-1}$
$p$	pressure, Pa
$\dot{Q}$	heat transfer rate, W
$R$	universal gas constant, $\text{J mol}^{-1} \text{ K}^{-1}$
$s$	volume fraction
$S$	source terms
$t$	time, s
$T$	temperature, K
$T_0$	volume averaged cell temperature, K

**Greek letters**

$\alpha$	transfer coefficient
$\varepsilon$	porosity
$\zeta$	water transfer rate, $\text{s}^{-1}$
$\eta$	overpotential, V
$\lambda$	water content in ionomer
$\xi$	stoichiometry ratio
$\rho$	density, $\text{kg m}^{-3}$
$\omega$	volume fraction of ionomer in catalyst layer
$\delta$	thickness, m

**Subscripts and superscripts**

$a$	anode
act	activation
amb	ambient
atm	atmosphere

BP	bipolar plate
$c$	cathode
cell	cell characteristic
channel	flow channel
CL	catalyst layer
conc	concentration
Cond	condensation
eff	effective
eq	equilibrium
$f$	frozen
fl	fluid phase
fmw	frozen membrane water
GDL	gas diffusion layer
$\text{H}_2$	hydrogen
$\text{H}_2\text{O}$	water
$i, j$	the $i$ th and $j$ th components
ice	ice
Kns	Knudsen diffusion coefficient
lq	liquid water
$l-i$	liquid water to ice (vice versa)
mem	membrane
nernst	Nernst
nf	non-frozen
nmw	non-frozen membrane water
$n-f$	non-frozen membrane water to frozen membrane water (vice versa)
$n-i$	non-frozen membrane water to ice (vice versa)
$n-v$	non-frozen membrane water to vapor (vice versa)
$\text{O}_2$	oxygen
ohmic	ohmic
out	outlet
pc	phase change
$r$	mean pore radius
ref	reference state
sat	saturation
sl	solid phase
$T$	energy (for source term)
vp	water vapor
wall	surrounding wall of the stack

further implemented the assisted catalytic hydrogen-oxygen reaction method in the multiphase cold start model, and found that successful start-up from  $-20^\circ\text{C}$  can be achieved with proper control of this method.

It should be noticed that even though the multi-dimensional multiphase cold start models for PEMFC can be used to investigate the various detailed transport phenomena, these models were only developed for single PEMFCs with single straight flow channels (only a small part of a practical single PEMFC) [21–27] or small stacks up to only 3 single cells [28] to the best of the authors' knowledge, although previous studies showed that the transport characteristics might be different at larger scales [19,20,28–31]. The main restriction of multi-dimensional multiphase cold start models for PEMFC is the limitation of computational power [28]. On the other hand, as mentioned previously, although one-dimensional models, requiring insignificant computational power, might be an alternative way to study the cold start characteristics of PEMFC stacks, these models often focused on the heat generation and transfer processes [19,20], and the coupled heat and mass transfer (e.g. ice formation and water transport) was often simplified. The major limitation of one-dimensional model is that the detailed transport phenomenon in the other two directions cannot

be taken into account, for example, the effect of detailed flow field structure [32] and water distributions cannot be considered. Higher dimensional models are needed to satisfy such requirements, and the results of previous multi-dimensional cold start models figured out these detailed transport phenomena for single PEMFCs [21–28]. However, for PEMFC stacks, considering the computational power limitation, and the fact that the through-plane transport plays the leading role, one-dimensional model is a reasonable choice for PEMFC stack modeling. Therefore, it is necessary to develop a one-dimensional (to be computationally efficient) large-scale cold start model considering the major heat and mass transfer processes for PEMFC stacks. With such a comprehensive stack model, the various assisted start-up methods can also be evaluated and analyzed in details.

In this study, a one-dimensional cold start model is developed for PEMFC stacks. This model accounts for the major transport phenomena during both the failed and successful cold start processes, such as the coupled water transport/phase change and heat transfer. Based on this model, a novel start-up method, variable heating and load control (VHLC), is proposed and evaluated. The transport characteristics during the different cold start processes in different PEMFC stacks are investigated.

## 2. Mathematical model

Fig. 1 shows the major transport phenomena considered in this stack model, including the water transport and phase change in membrane, catalyst layer (CL) and gas diffusion layer (GDL), and heat generation/transfer in different components. The heat and mass transfer along the direction normal to the membrane surface (the through-plane direction) is considered in this one-dimensional model (defined as the  $x$ -direction in this model). The design and operating parameters are given in Table 1.

### 2.1. Water transport

In this model, for the water transport in the membrane and in the electrolyte of CL, the mass conservation equations of non-frozen and frozen membrane water are solved along the through-plane direction ( $x$ -direction):

(Table 2).  $S_{nmw}$  and  $S_{fmw}$  are the source terms of non-frozen membrane water and frozen membrane water, respectively, as shown in Table 3. The source term of non-frozen membrane water includes the product water from the reaction, water phase change, and migrated water due to the electro-osmotic drag (EOD) effect. The source term of frozen membrane water includes the phase change between frozen and non-frozen membrane water. These assumptions of water phase change were proposed in previous work for single PEMFC modeling [25]. In the pores of CL and GDL, the mass conservation equations of liquid water and ice are solved along the through-plane direction ( $x$ -direction):

$$\text{Liquid water : } \frac{\partial(\varepsilon \rho_{lq} \cdot s_{lq})}{\partial t} = \frac{\partial^2(\rho_{lq} D_{lq} \cdot s_{lq})}{\partial x^2} + S_{lq} \quad (3)$$

$$\text{Non – frozen membrane water : } \frac{\rho_{mem}}{EW} \cdot \frac{\partial(\omega \lambda_{nf})}{\partial t} = \frac{\rho_{mem}}{EW} \cdot \frac{\partial^2(\omega^{1.5} D_{nmw} \lambda_{nf})}{\partial x^2} + S_{nmw} \quad (1)$$

$$\text{Frozen membrane water : } \frac{\rho_{mem}}{EW} \frac{\partial(\omega \lambda_f)}{\partial t} = S_{fmw} \quad (2) \quad \text{Ice : } \frac{\partial(\varepsilon s_{ice} \rho_{ice})}{\partial t} = S_{ice} \quad (4)$$

where  $\rho$  ( $\text{kg m}^{-3}$ ) is the density,  $EW$  ( $\text{kg kmol}^{-1}$ ) the equivalent weight of membrane,  $\omega$  the volume fraction of ionomer in CL,  $\lambda$  the water content in ionomer, and  $D$  ( $\text{m}^2 \text{s}^{-1}$ ) the mass diffusivity

where  $\varepsilon$  is the porosity, and  $s$  the volume fraction. Since the convective mass transfer in GDL and CL is only considerable with cross-flow along the in-plane directions [33], only diffusive mass

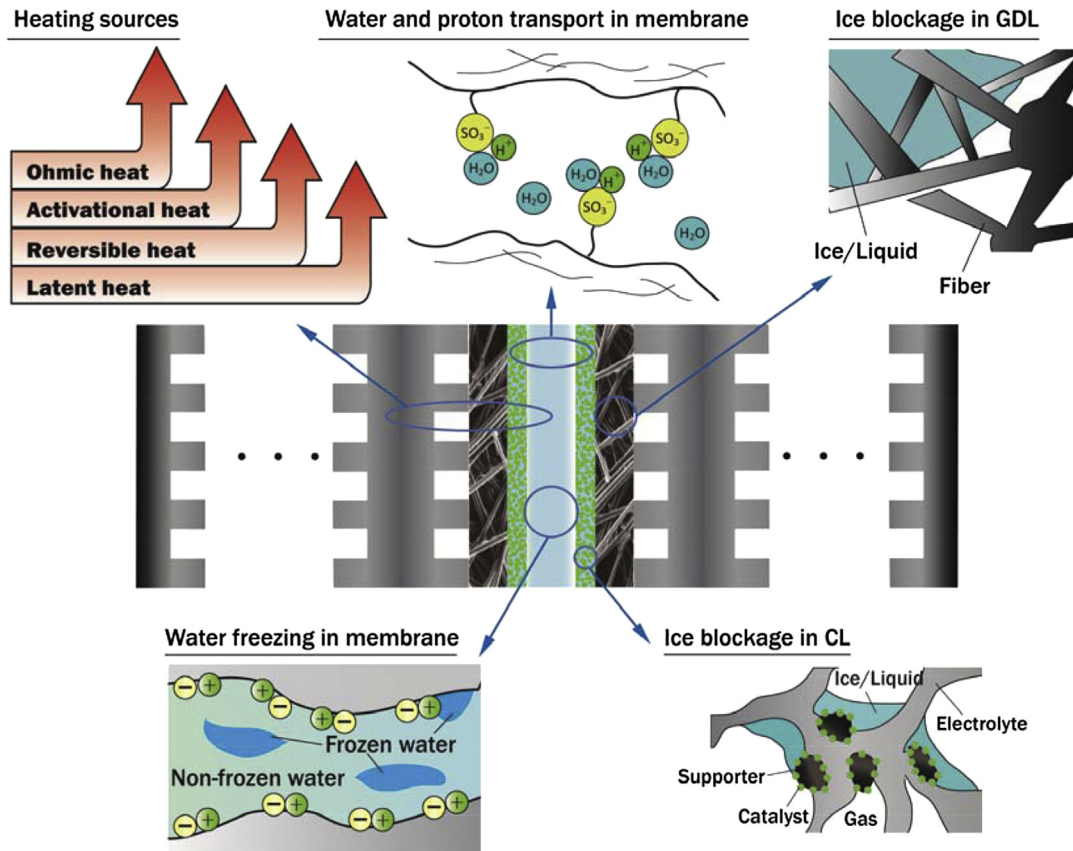


Fig. 1. Major transport phenomena considered in this stack model.

**Table 1**  
Design and operating parameters.

Parameters	Value
Effective reaction area	100 cm <sup>2</sup>
Thickness of BP	2 mm
Depth of channel	1 mm
Thicknesses of membrane; CL; GDL	0.03 mm; 0.01 mm; 0.2 mm
Intrinsic permeabilities of CL; GDL	$K_{CL} = 6.2 \times 10^{-13} \text{ m}^2$ ; $K_{GDL} = 6.2 \times 10^{-12} \text{ m}^2$
Densities of membrane; CL; GDL; BP	$\rho_{\text{mem,CL,GDL,BP}} = 1980; 1000; 1000; 1000 \text{ kg m}^{-3}$
Specific heat capacities of membrane; CL; GDL; BP	$(C_p)_{\text{mem,CL,GDL,BP}} = 833; 3300; 568; 1580 \text{ J kg}^{-1} \text{ K}^{-1}$
Thermal conductivities of membrane; CL; GDL; BP	$k_{\text{mem,CL,GDL,BP}} = 0.95; 1.0; 1.0; 20 \text{ W m}^{-1} \text{ K}^{-1}$
Electric conductivities of CL; GDL; BP	$\kappa_{\text{CL,GDL,BP}} = 300; 300; 20000 \text{ S m}^{-1}$
Volume fraction of ionomer ( $\omega$ ) in CL	$\omega = 0.3$ ;
Porosities ( $\epsilon$ ) of CL; GDL	$\epsilon_{\text{CL,GDL}} = 0.3; 0.6$
Stoichiometry ratio	$\xi_{a,c} = 2.0$
Relative humidities of inlet gases	$RH_{a,c}^{\text{in}} = 0$
Inlet gas and surrounding temperatures	$T_{a,c}^{\text{in}} = T_{\text{surr}} = -20^\circ \text{C}$
Initial stack temperature	$T_{\text{init}} = T_{\text{surr}} = -20^\circ \text{C}$
Pressure at outlets	$p_{a,c}^{\text{out}} = 1 \text{ atm}$
Heat transfer coefficients on endplate surfaces	$h = 100 \text{ W m}^{-2} \text{ K}^{-1}$ or $h = 0 \text{ W m}^{-2} \text{ K}^{-1}$
Heat transfer coefficients on side surfaces	$h = 2 \text{ W m}^{-2} \text{ K}^{-1}$
Initial ice volume fraction	0
Initial non-frozen water content in ionomer	2.5
Initial frozen water content in ionomer	0

transfer is considered in this one-dimensional model along the through-plane direction. The related transport properties are given in Table 2. The source terms consider the water phase change, as shown in Table 3. The water vapor transport is also considered to be the diffusion dominated along the through-plane direction, and the average water vapor concentration in CL and GDL is updated directly at each time step rather than solving a partial differential equation. In fact, during the cold start processes, the water vapor amount is very low due to the low water saturation pressure. Such low water vapor amount has insignificant effect on the cold start processes (this was also reported in previous studies [25,26,33]). Therefore, the water vapor transport is further simplified to improve the calculation efficiency. For water vapor in CL:

$$c_{\text{vp,CL}}^t = c_{\text{vp,CL}}^{t-\Delta t} + \zeta(\lambda_{\text{CL}} - \lambda_{\text{CL}}^{\text{eq}}) \frac{\rho_{\text{mem}} \Delta t}{EW} - \frac{(c_{\text{CL}}^{t-\Delta t} - c_{\text{GDL}}^{t-\Delta t}) D_{\text{CL-GDL}}^{\text{eff}} \Delta t}{(\delta_{\text{CL}}/2) + (\delta_{\text{GDL}}/2) \delta_{\text{CL}} \epsilon_{\text{CL}}} \quad (5)$$

where  $c$  (mol m<sup>-3</sup>) is the concentration,  $t$  (s) the time step,  $\Delta t$  (s) the time step size,  $\zeta$  (s<sup>-1</sup>) the water transfer rate,  $\delta$  (m) the thickness,  $\xi$  the stoichiometry ratio, and  $D$  (m<sup>2</sup> s<sup>-1</sup>) the effective diffusion coefficient corrected by the ice and liquid volume fraction in CL and GDL (Table 2). The second term on the right hand side of Equation (5) represents the water absorption/desorption by the ionomer in CL, and the third term is for water diffusion between CL and GDL. For water vapor in GDL:

**Table 2**  
Correlations for different water transport properties [22,25,33,35].

Parameters	Value
Membrane water diffusivity (m <sup>2</sup> s <sup>-1</sup> )	$D_{\text{nmw}} = \begin{cases} 2.69266 \times 10^{-10} (\lambda \leq 2) \\ 10^{-10} \cdot \exp[2416(\frac{1}{303} - \frac{1}{T})] \cdot [0.87 \cdot (3 - \lambda_{\text{nf}}) + 2.95 \cdot (\lambda_{\text{nf}} - 2)], & (2 < \lambda_{\text{nf}} \leq 3) \\ 10^{-10} \cdot \exp[2416(\frac{1}{303} - \frac{1}{T})] \cdot [2.95 \cdot (4 - \lambda_{\text{nf}}) + 1.642454 \cdot (\lambda_{\text{nf}} - 3)], & (3 < \lambda_{\text{nf}} \leq 4) \\ 10^{-10} \cdot \exp[2416(\frac{1}{303} - \frac{1}{T})] \cdot [2.563 - 0.33 \cdot \lambda_{\text{nf}} + 0.0264 \cdot \lambda_{\text{nf}}^2 - 0.000671 \cdot \lambda_{\text{nf}}^3], & (\lambda_{\text{nf}} > 4) \end{cases}$
Liquid water diffusivity (m <sup>2</sup> s <sup>-1</sup> )	$D_{\text{liq}} = -\frac{K_{\text{liq}}}{\mu_{\text{liq}}} \frac{dp_{\text{v}}}{ds_{\text{liq}}}$ $K_{\text{liq}} = K_{\text{CL,GDL}}^0 s_{\text{liq}}^4 (1 - s_{\text{ice}})^4$
Water vapor diffusivity in CL (m <sup>2</sup> s <sup>-1</sup> )	$D_{\text{CL}}^{\text{eff}} = D_{\text{v}} \epsilon^{1.5} (1 - s_{\text{liq}}^{\text{CL}} - s_{\text{ice}}^{\text{CL}})^{1.5}$ $D_{\text{v}} = 2.982 \times 10^{-5} \left( \frac{T}{333.15} \right)^{1.5} \left( \frac{101325}{p} \right)$
Water vapor diffusivity in GDL (m <sup>2</sup> s <sup>-1</sup> )	$D_{\text{GDL}}^{\text{eff}} = D_{\text{v}} \epsilon^{1.5} (1 - s_{\text{liq}}^{\text{GDL}} - s_{\text{ice}}^{\text{GDL}})^{1.5}$

**Table 3**  
Source terms for water conservation equations.

Parameters	Value
Non-frozen membrane water source terms (kmol m <sup>-3</sup> s <sup>-1</sup> )	$S_{nmw} = \begin{cases} -S_{n-f} & (\text{in membrane}) \\ \frac{j_c}{2F} - S_{n-v} - S_{n-i} + S_{EOD} & (\text{in cathode CL}) \\ -S_{n-v} - S_{n-i} + S_{EOD} & (\text{in anode CL}) \end{cases}$
Frozen membrane water source terms (kmol m <sup>-3</sup> s <sup>-1</sup> )	$S_{fmw} = S_{n-f}$
Liquid water source terms (kg m <sup>-3</sup> s <sup>-1</sup> )	$S_{lq} = S_{l-i} + S_{n-i} M_{H_2O}$
Ice source terms (kg m <sup>-3</sup> s <sup>-1</sup> )	$S_{ice} = \begin{cases} S_{l-i} + S_{n-i} M_{H_2O} & (\text{in CL}) \\ S_{l-i} & (\text{in GDL}) \end{cases}$

$$c_{vp,GDL}^t = c_{vp,GDL}^{t-\Delta t} + \frac{(c_{CL}^{t-\Delta t} - c_{GDL}^{t-\Delta t}) D_{CL-GDL}^{eff} \Delta t}{(\delta_{CL}/2) + (\delta_{GDL}/2) \delta_{CL} \epsilon_{CL}} - \frac{(c_{GDL}^{t-\Delta t} - c_{channel}) D_{GDL}^{eff} \Delta t}{\delta_{GDL}/2 \delta_{GDL} \epsilon_{GDL}} \quad (6)$$

where the second and third terms on the right hand side of Equation (6) represent the water diffusion between CL and GDL and between GDL and flow channel, respectively. As mentioned previously, since the water removed as vapor counts only a very small proportion of product water (this was also reported in previous studies [25,26,33]), it is assumed that the water vapor is taken away instantaneously in the flow channel, therefore the water vapor concentration in flow channel ( $c_{channel}$ ) is considered to be zero in this model.

## 2.2. Heat transfer

The one-dimensional heat transfer along the through-plane direction ( $x$ -direction) with different heating sources is considered in this model:

$$\text{Energy conservation: } \frac{\partial}{\partial t} ((\rho C_p)^{eff} T) = \frac{\partial^2 (k_{fl,sl}^{eff} T)}{\partial x^2} + S_T \quad (7)$$

where  $C_p$  (J kg<sup>-1</sup> K<sup>-1</sup>) is the specific heat,  $T$  (K) the temperature, and  $k$  (W m<sup>-1</sup> K<sup>-1</sup>) the thermal conductivity. The convective heat transfer along the through-plane direction is neglected, since it is often insignificant by comparing with the conductive heat transfer. The effective density, heat capacity and thermal conductivity are calculated based on the stack materials and ice/liquid/gas concentrations. The heating sources in the different components include the activation heat, ohmic heat, reversible heat and latent heat, as demonstrated in Fig. 1. The source term is expressed as

$$S_T = \begin{cases} j_c \eta_{act} + \frac{I^2 ASR_{CL}}{3 \delta_{CL}} + S_{pc} & (\text{in anode CL}) \\ -\frac{j_c T \Delta S}{2F} + j_c \eta_{act} + \frac{I^2 ASR_{CL}}{3 \delta_{CL}} + S_{pc} & (\text{in cathode CL}) \\ \frac{I^2 ASR_{GDL}}{\delta_{GDL}} + S_{pc} & (\text{in GDL}) \\ \frac{I^2 ASR_{BP}}{\delta_{BP}} & (\text{in BP}) \\ \frac{I^2 ASR_{mem}}{\delta_{mem}} + S_{pc} & (\text{in membrane}) \\ 0 & (\text{in other zones}) \end{cases} \quad (8)$$

where ASR (Ω m<sup>2</sup>) is the area specific resistance,  $\eta$  (V) the overpotential, and  $j$  (A m<sup>-2</sup>) the reaction rate. Since the average reaction

rate is used in this model, the reaction rate is calculated as the ratio of the current density ( $I$ , A m<sup>-2</sup>) and CL thickness ( $\delta_{CL}$ , m). The relationship between the current density and stack voltage is discussed in the next subsection.

## 2.3. Performance prediction

In this model, the charge conservation equation is not solved, and as the alternative, the performance is calculated analytically based on the Tafel representation [34] and the transport parameters during the cold start processes. The output voltage can be calculated as

$$V_{out} = V_{Nernst} + V_{act} + V_{conc} + V_{ohmic} \quad (9)$$

The first term on the right hand side of Equation (9) is the open circuit voltage (OCV), which is calculated by the Nernst equation:

$$V_{Nernst} = 1.23 - 0.9 \times 10^{-3} (T - T_0) + \frac{RT_0}{2F} \ln \left( \frac{p_{H_2} p_{O_2}}{p_{H_2O}} \right) \quad (10)$$

where  $R$  (J mol<sup>-1</sup> K<sup>-1</sup>) is the universal gas constant, and  $T_0$  is a constant of 298.15 K. The second term on the right hand side of Equation (9) is the activation voltage loss:

$$V_{act} = -b \ln \left( \frac{I}{(1 - s_{ice} - s_{lq})^{0.5} j_*^h} \right) \quad (11)$$

$$b = \frac{RT}{\alpha F} \quad (12)$$

$$j_*^h = j_* \delta_{CL} \left( \frac{c_h}{c_{ref}} \right) \quad (13)$$

$$c_h = \frac{1 + (1 - 1/\xi) 0.21 p_c}{2 RT} \quad (14)$$

where  $b$  is the Tafel slope,  $I$  (A cm<sup>-2</sup>) is the current density,  $j_*^h$  (A cm<sup>-2</sup>) is the reference current density. Therefore, the effects of reactant concentration and ice/liquid formation on the activation voltage loss are all considered. The third term on the right hand side of Equation (9) is the voltage loss due to the reactant transport:

$$V_{conc} = b \ln \left( 1 - \frac{I}{j_D} \right) \quad (15)$$

$$j_D = \frac{4 F c_h}{\delta_{GDL} / D_{GDL}^{eff} + 0.5 \delta_{CL} / D_{CL}^{eff}} \quad (16)$$

The fourth term on the right hand side of Equation (9) is the ohmic voltage loss:

$$V_{ohmic} = -ASR \cdot j \quad (17)$$

where the area specific resistance (ASR) is calculated as

$$ASR = A_{cell} (R_{mem} + R_{CL} + R_{GDL} + R_{BP}) \quad (18)$$

The resistance of membrane is calculated based on the correlation provided by Springer et al. [35], and the resistance of CL includes both the ionomer (for proton transport) and catalyst (for electron transport).



#### 2.4. Boundary and initial conditions

For the surrounding walls of the stack, the convective heat transfer condition is set as:

$$\dot{Q} = hA(T_{\text{amb}} - T_{\text{wall}}) \quad (19)$$

where  $h$  ( $\text{W m}^{-2} \text{K}$ ) is the heat transfer coefficient,  $A$  ( $\text{m}^2$ ) the surface area,  $T_{\text{amb}}$  (K) the ambient temperature, and  $T_{\text{wall}}$  (K) the wall temperature. The heat transfer coefficient is set to be  $2 \text{ W m}^{-2} \text{K}$  on the side walls except the end plates, to reflect a well insulation condition on these walls (nature convection condition). On the end plates, different heat transfer coefficients are considered, as given in Table 1. External heating is also applied to different cells for the assisted cold start processes.

To calculate the cell output voltage at a current density (constant current condition), the current density of each cell is considered as a constant:

$$I_{\text{cell } i} = \text{Constant} \quad (20)$$

where  $i$  represents the  $i$ th cell. The total stack output voltage is the sum of all cell voltages (can be calculated by using Equation (9)). For the constant voltage condition, the total voltage of the different cells is a constant:

$$\sum_i^N V_{\text{out } i} = V_{\text{out\_stack}} = \text{Constant} \quad (21)$$

For a stack with  $N$  cells, the following equation system is solved:

$$\begin{bmatrix} V_{\text{out}_1} = & \text{Fun}_{\text{Tafel}} & (I, [\text{Parameters}_1]) \\ & \dots & \dots \\ V_{\text{out}_i} = & \text{Fun}_{\text{Tafel}} & (I, [\text{Parameters}_i]) \\ & \dots & \dots \\ V_{\text{out}_N} = & \text{Fun}_{\text{Tafel}} & (I, [\text{Parameters}_N]) \\ \sum_i^N V_{\text{out } i} = & V_{\text{out\_stack}} & \end{bmatrix} \quad (22)$$

where  $\text{Fun}_{\text{Tafel}}$  is the performance equation (Equation (9)), and  $I$  ( $\text{A m}^{-2}$ ) is the current density (one of the unknowns).  $\text{Parameters}_i$  is the state parameters of the  $i$ th individual cell such as temperature and ice volume fraction.  $V_{\text{out } i}$  (V) is the output cell voltage of the  $i$ th cell (one of the unknowns). Therefore, the current density and the voltages of different cells can be calculated.

The initial temperature is set as the same with the ambient temperature of  $-20^\circ \text{C}$ , the initial water content in ionomer is 2.5 to reflect the well purged condition before the cold start processes, and the initial ice volume fraction is 0.

#### 2.5. Numerical methods

In this study, the membrane water, liquid, ice and energy conservation equations are solved. The finite volume method is used to discretize these differential equations. There are totally 250 grid nodes for each cell, and the distributions for the different components are 30, 20, 20, 30 and 50 nodes for the bipolar plate (BP), flow channel, GDL, CL and membrane, respectively. In each discretized control volume, the equations are solved with the fourth-order Runge–Kutta method. Explicit time discretization is used, and adaptive time step using the Dormand–Prince pair for error estimation is adopted for the automatic adjustment of iteration time step. Grid independent study has been carefully carried out to ensure that further increasing the number of grid has negligible

influence on the results. To solve Equation (22) for the constant voltage condition, the algorithm of Levenberg–Marquardt [36] is used with the second order accuracy. The termination tolerance is set as  $10^{-9}$ , which means that the convergence completes once the errors become less than  $10^{-9}$ .

### 3. Results and discussion

Fig. 2 shows the comparison between the present model prediction and experimental data in Ref. [37] for the cold start processes starting from  $-20^\circ \text{C}$  at 3 different current densities. For this comparison, the model parameters are set according to the experimental conditions in Ref. [37]. It can be noticed that the agreement is reasonable for the whole cold start processes.

In this section, the unassisted cold start characteristics of different PEMFC stacks are discussed first, and the effects of number of cells in stacks and start-up modes (constant current and constant voltage) are investigated. The external heating assisted cold start processes are then analyzed, and the external heating method is optimized to improve the cold start performance. A novel start-up method, variable load and heating control (VLHC), is proposed and evaluated as well. As shown in Table 1, a typical start-up temperature,  $-20^\circ \text{C}$ , is considered for all the cold start processes; the inlet gases are also at  $-20^\circ \text{C}$  and the relative humidity is 0; the initial water content in electrolyte is 2.5 and there is no ice at the beginning of the cold start processes; the start-up current density/voltage are  $0.1 \text{ A cm}^{-2}$ ,  $0.15 \text{ A cm}^{-2}$  and  $0.3 \text{ V}$ ; and the operating pressure is 1 atm. At the two end surfaces, forced convection with a heat transfer coefficient of  $100 \text{ W m}^{-2} \text{K}^{-1}$  is considered, and at the other outer surfaces, a heat transfer coefficient of  $2 \text{ W m}^{-2} \text{K}^{-1}$  is considered representing the nature convection condition. The heat transfer coefficient can also be changed to 0 representing the heat insulation condition. For the external heating condition, a heating power of 100 W is applied for different cells in the 20-cell stack to optimize the cold start performance.

#### 3.1. Effect of number of cells

Fig. 3 shows the effect of stack cell numbers (total amount of cells in a stack) on the time durations and final volume averaged stack temperatures for the failed unassisted cold start processes from  $-20^\circ \text{C}$  at  $0.1 \text{ A cm}^{-2}$ . For the stacks with more cells, the start-up process can last longer and the final temperature reached is

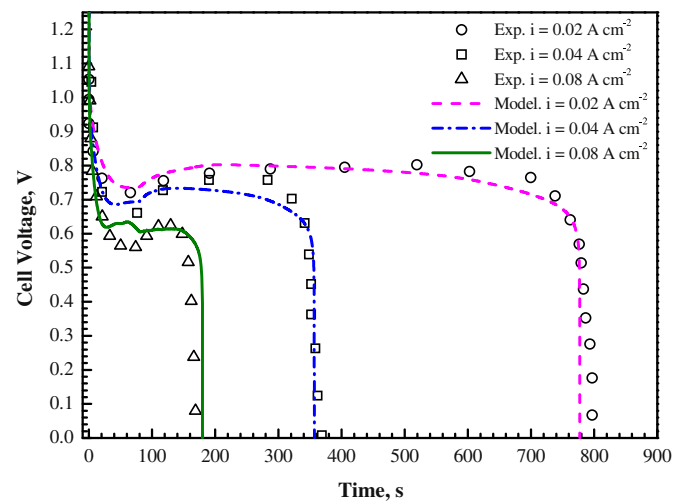
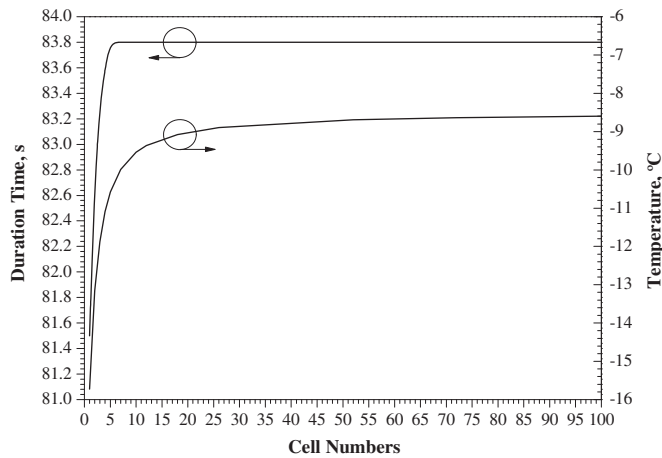


Fig. 2. Comparison between the present model predictions and experimental data (experimental data from Ref. [37]).



**Fig. 3.** Effect of number of cells (total amount of cells in a stack) on the time durations and final volume averaged stack temperatures for the failed unassisted cold start processes from  $-20\text{ }^{\circ}\text{C}$  at  $0.1\text{ A cm}^{-2}$ .

higher, because a stack with more cells reduces the outer surface area, resulting in better heat insulation. However, this effect becomes less significant by further increasing the amount of cells. The start-up durations and final temperatures are similar for the stacks with more than 20 cells.

The temperature distributions in the stacks with different amounts of cells (stack with 1 cell represents single cell) at the end in of the failed unassisted cold start processes from  $-20\text{ }^{\circ}\text{C}$  at  $0.1\text{ A cm}^{-2}$  are shown in Fig. 4. For the different stacks, the cells in the middle have the highest temperature, on the other hand, the peak temperatures can be observed around the membrane in different cells, because most of the heat is produced there. The temperature differences between the cells on the side and in the middle are larger for the stacks with more cells.

For the 20-cell stack starting from  $-20\text{ }^{\circ}\text{C}$  at  $0.1\text{ A cm}^{-2}$ , the ice volume fractions in the cathode CLs of different cells at the end of the failed unassisted cold start process is shown in Fig. 5. The cells at the two ends have slightly more ice than the middle cells, mainly due to the lower temperatures (Fig. 4) there. The 10 cells in the middle have almost the same amount of ice. Generally, the ice amounts in the different cells of the stack are similar.

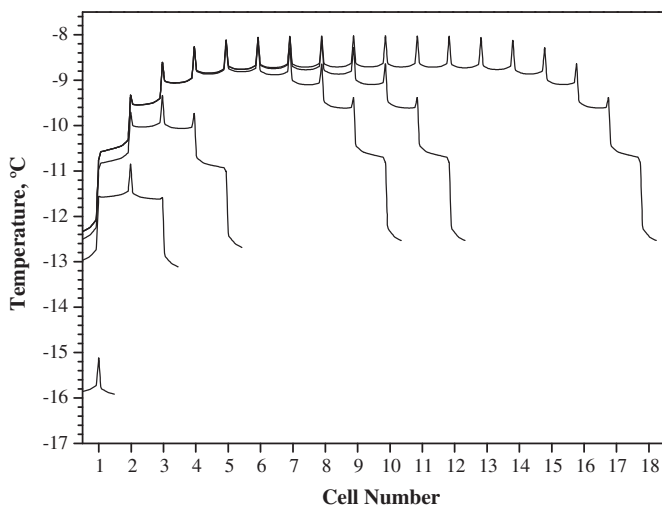


**Fig. 4.** Temperature distributions in the stacks with different amounts of cells (stack with 1 cell represents single cell) at the end in of the failed unassisted cold start processes from  $-20\text{ }^{\circ}\text{C}$  at  $0.1\text{ A cm}^{-2}$ .

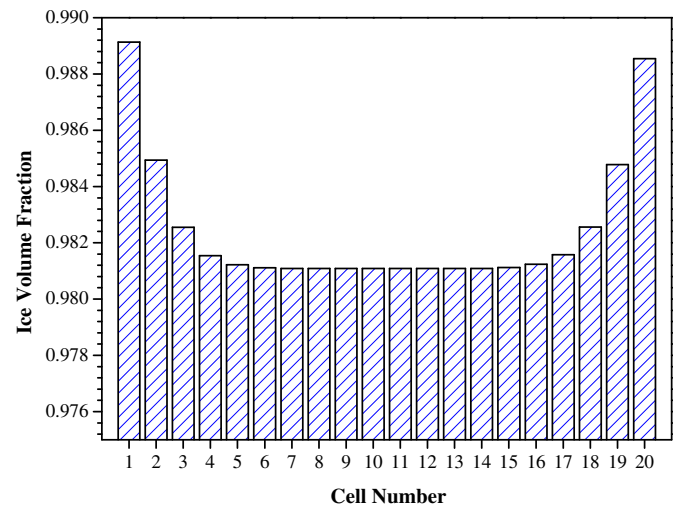


**Fig. 5.** Ice volume fractions in the cathode CLs of different cells in the 20-cell stack at the end of the failed unassisted cold start process from  $-20\text{ }^{\circ}\text{C}$  at  $0.1\text{ A cm}^{-2}$ .

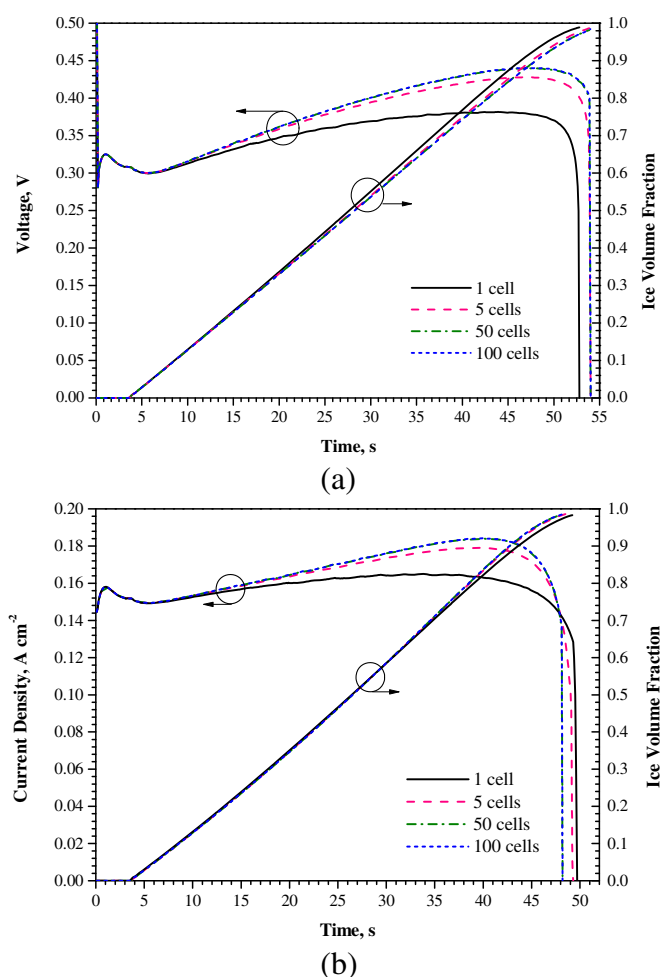
### 3.2. Effect of start-up current/voltage

Fig. 6 shows the evolutions of average cell voltage/current density and average ice volume fraction in cathode CLs of different stacks starting from  $-20\text{ }^{\circ}\text{C}$ . For the constant current start-up mode at  $0.15\text{ A cm}^{-2}$  (Fig. 6(a)), the voltage is the average value of the different cells in the stack. The voltages are initially almost the same for the different stacks with different amounts of cells. After about 10 s, the difference in voltage becomes noticeable, and the stacks with more cells have higher voltages, due to the higher temperatures caused by the better heat insulation, as discussed previously with Figs. 3 and 4. Moreover, the voltage difference is larger between the 5-cell stack and single cell than between the 100-cell stack and 5-cell stack, following the same trend of the stack temperature shown in Fig. 3. The ice volume fractions are quite similar for the different stacks during the whole process, and the stacks with more cells only have slightly slower ice formation processes. For the constant voltage mode (Fig. 6(b)), it can be noticed that for the stacks with slightly lower ice formation rates (smaller stacks), the current densities are lower, and correspondingly the start-up processes last slightly longer. These trends are opposite to Fig. 6(a) with constant current density. Because the larger stacks in Fig. 6(b) (higher average temperatures as discussed previously) lead to higher current densities during the start-up processes, causing more water generation and ice formation.

The ice volume fractions in the cathode CLs of different cells in the 50-cell stack during the failed unassisted cold start processes from  $-20\text{ }^{\circ}\text{C}$  at  $0.15\text{ A cm}^{-2}$  and at  $0.3\text{ V}$  are shown in Fig. 7. For both the constant current and constant voltage start-up processes, the ice distributions are similar, with slightly more ice on the sides, and the ice amounts in the different cells are generally similar during the whole start-up processes, which is also consistent with the results shown in Fig. 5. The ice volume fraction discrepancies among the side cells and middle cells become more notable during the cold start processes, and this agrees with the trend of the stack temperature distribution shown in Fig. 4.

### 3.3. External heating and variable heating and load control (VHLC)

In order to improve the cold start performance of PEMFC stack, external heating combined with thermal insulation is performed and optimized based on a 20-cell stack. The optimization is focused



**Fig. 6.** Evolutions of average cell voltage/current density and average ice volume fraction in cathode CLs of different stacks starting from  $-20^{\circ}\text{C}$  at (a)  $0.15\text{ A cm}^{-2}$  and (b)  $0.3\text{ V}$ .

on the control of the heating location and the load on the active cells, so called the variable heating and load control (VHLC). To compare the different cases consistently, the total external heating power is set as a constant of  $100\text{ W}$  (around 20% of the power that the 20-cell stack can generate in normal operation), which can be supplied by an auxiliary power source such as a super capacitor or a battery.

Fig. 8 shows the evolutions of stack voltage and average ice volume fraction in cathode CLs. The external heating is performed uniformly on each individual cell, and for comparison, the cold start processes with/without external heating and with/without thermal insulation on the endplate surfaces are all considered. With external heating, the ice formation process is slower, the stack voltage is higher, and the cold start process lasts longer. The thermal insulation improves the cold start performance less significantly than the external heating. However, all the cold start processes shown in Fig. 8 are finally failed. Therefore, for successful cold start, either the external heating power needs to be increased, or the heating method needs to be optimized.

A novel variable heating and load control (VHLC) method is proposed in this study. The main idea of this method is to only apply load to the still-active cells (not fully covered by ice), and to simultaneously apply external heating to certain cells inside stack. This method can be easily implemented by placing the external heating pads at different locations of the stack and modifying the

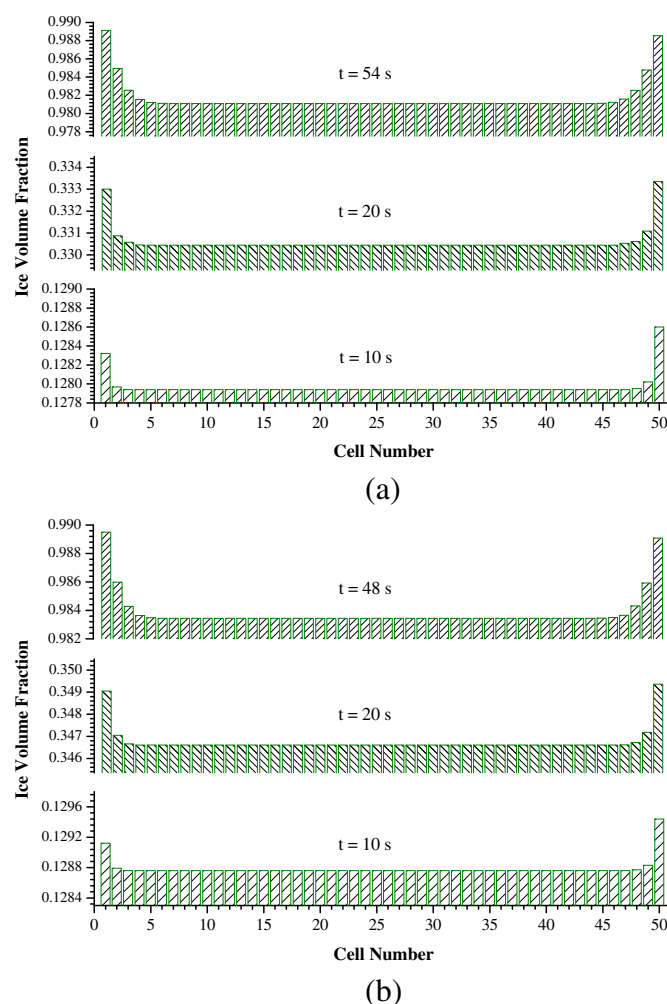


**Fig. 7.** Ice volume fractions in cathode CLs of different cells in the 50-cell stack during the failed unassisted cold start processes from  $-20^{\circ}\text{C}$  at (a)  $0.15\text{ A cm}^{-2}$  and (b)  $0.3\text{ V}$ .

external circuits. Based on this method, the external heating power is expected to be used more efficiently, and the stack self-heating ability is expected to be enhanced. The still-active cells assisted by the external heating power may start-up successfully and eventually melt the ice in the dead cells (cells fully blocked by ice). To examine this method, the same heating power of  $100\text{ W}$  is used to compare with the results in Fig. 8.

By comparing with Fig. 8, the cold start process in Fig. 9 has thermal insulation on the endplate surfaces, and the external heating is applied on the two end cells on both sides of the stack. The evolutions of the stack voltage and the ice volume fractions of the three cells at different locations of the stack are shown in Fig. 9(a). It can be noticed that the stack successfully starts up from  $-20^{\circ}\text{C}$ , though a period with relatively low stack voltage. In the first 50 s, the stack voltage keeps increasing, because the membranes are humidified by the product water and the CLs are not fully covered by ice yet. At about 50 s, the stack voltage sharply decreases by about  $7.2\text{ V}$ , because most of the cells failed at almost the same time, which can be indicated from the ice volume fraction curves for Cell 5 (5 cells away from the endplate) and Cell 10 (in the middle of the stack). The stack voltage starts increasing again at about 60 s, and the step increment is about  $0.5\text{ V}$  for about every 14 s, indicating that the dead cells are active again one by one. For the ice distribution in Fig. 9(b), it can be observed that the ice volume fractions in the 16 middle cells are almost the same and



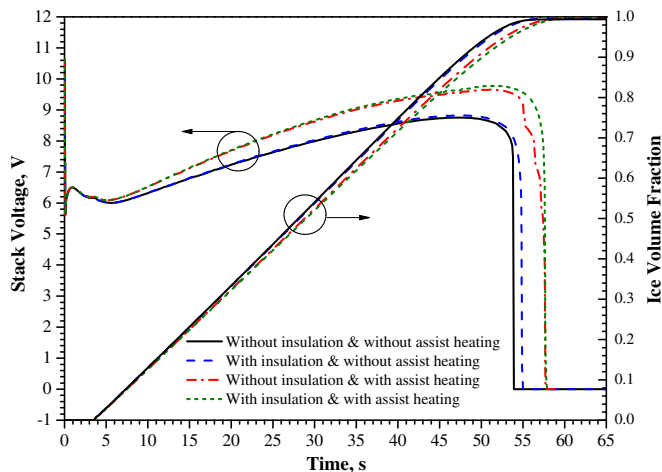


**Fig. 8.** Evolutions of stack voltage and average ice volume fraction in cathode CLs of the 20-cell stack starting from  $-20\text{ }^{\circ}\text{C}$  at  $0.15\text{ A cm}^{-2}$  with the two end surfaces with/without thermal insulation and with/without external heating (external heating is evenly distributed on each individual cell).

become 1 all at about 50 s. On the other hand, the 4 cells at the two ends of the stack keep working due to the external heating. For the temperature distribution in Fig. 9(c), the temperatures are the highest at the two ends of the stack due to the external heating. However, it takes about 245 s to melt the ice in the middle cell.

By comparing with Fig. 9, the change in Fig. 10 is that the external heating is applied to the individual cell in the middle of the stack (Cell 10). Accordingly, the ice starts melting in Cell 10 first. It is suggested that the cold start process in Fig. 10 is more optimal than Fig. 9, because the lowest stack voltage during the cold start process in Fig. 9 is about 2.2 V, and it is about 2.8 V in Fig. 10, indicating that there is one more cell working.

It can be noticed that the 6 cells in the middle are always active during the cold start process in Fig. 10. Therefore, for the cold start process in Fig. 11, the external heating is evenly distributed to the 6 middle cells. The lowest stack voltage is about 3.4 V during the cold start process in Fig. 11, which is about 0.6 V higher than the one in Fig. 10, indicating that the number of cells working is increased. In addition, the total time for every cell to reach  $0\text{ }^{\circ}\text{C}$  is reduced for more than 10 s, and the temperature is more evenly distributed for the cold start process in Fig. 11.

The results in Figs. 8–11 demonstrate that with the same external heating power, the novel variable heating and load control (VHLC) method can improve the cold start performance significantly, which is critically important for PEMFC in automotive applications.

#### 4. Conclusion

In this study, a cold start model for proton exchange membrane fuel cell (PEMFC) stacks is developed, and a novel start-up method, variable heating and load control (VHLC), is proposed and evaluated. The main idea is to only apply load to the neighboring still-active cells, and to apply external heating to certain cells inside the stack simultaneously (load is not applied to the cells fully blocked by ice, although these cells can gain heat from neighboring cells). Simulations of the cold start processes from  $-20\text{ }^{\circ}\text{C}$  are performed, with the initial water content in ionomer of 2.5 (representing the well purged condition before the cold start processes), and the initial ice volume fraction of 0. The results show that the stacks with more cells can reach higher temperatures, and for the stacks with more than 20 cells, this effect becomes

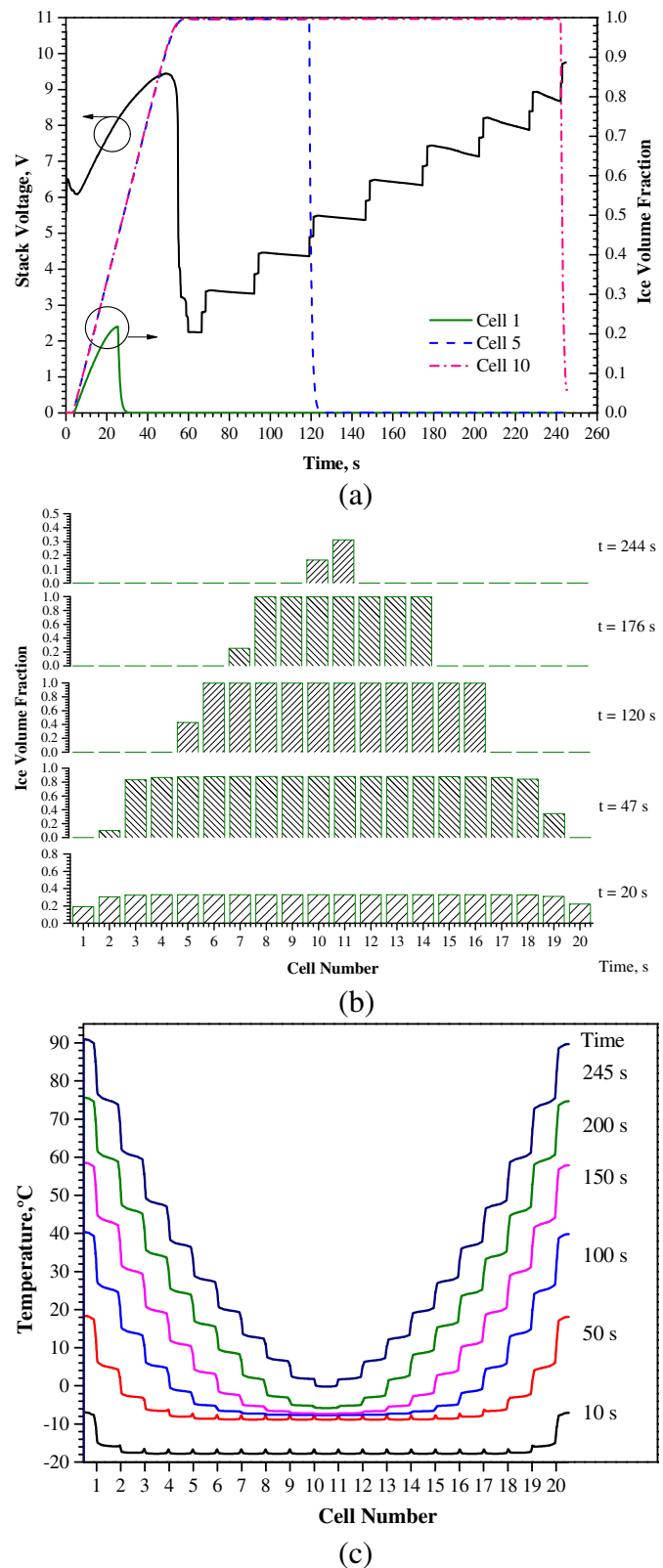
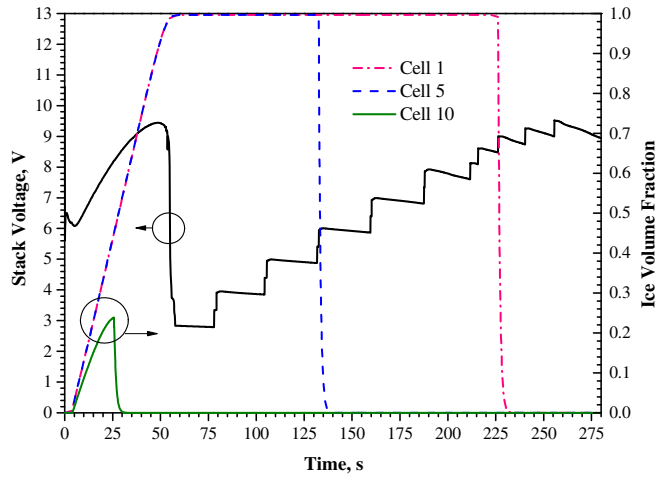
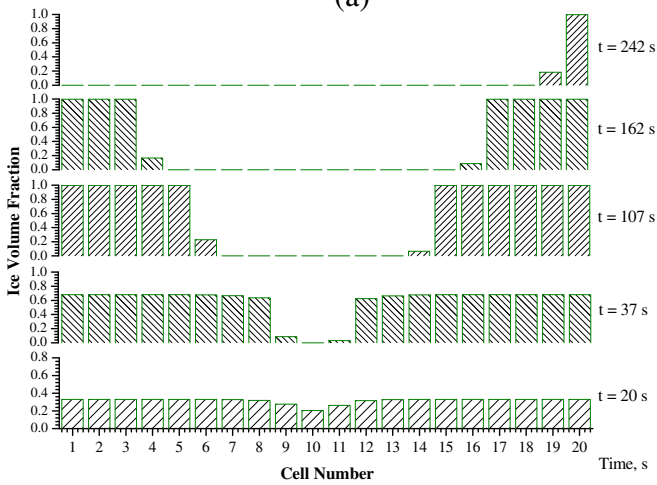


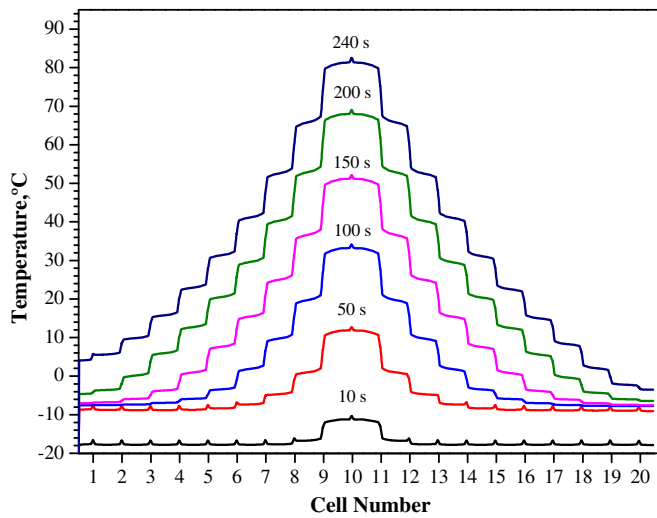
**Fig. 9.** Evolutions of (a) stack voltage and average ice volume fraction in cathode CLs, (b) ice volume fractions in cathode CLs of different cells, and (c) temperature distributions of the 20-cell stack starting from  $-20\text{ }^{\circ}\text{C}$  at  $0.15\text{ A cm}^{-2}$  with the two end surfaces thermally insulated and with an external heating power of 100 W (external heating is applied to the two end cells on both sides).



(a)

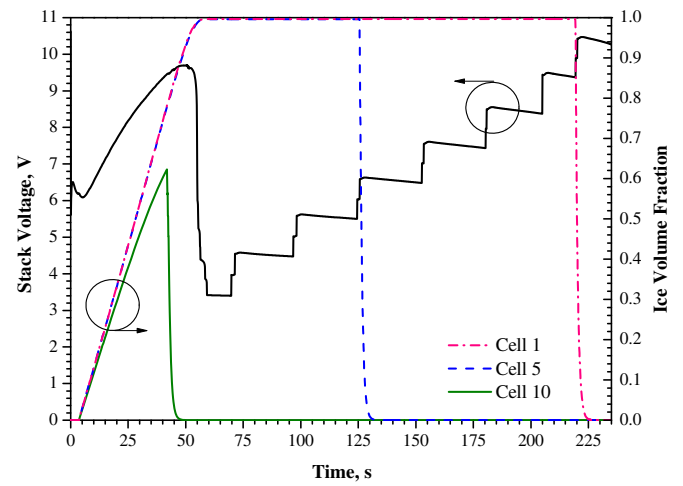


(b)

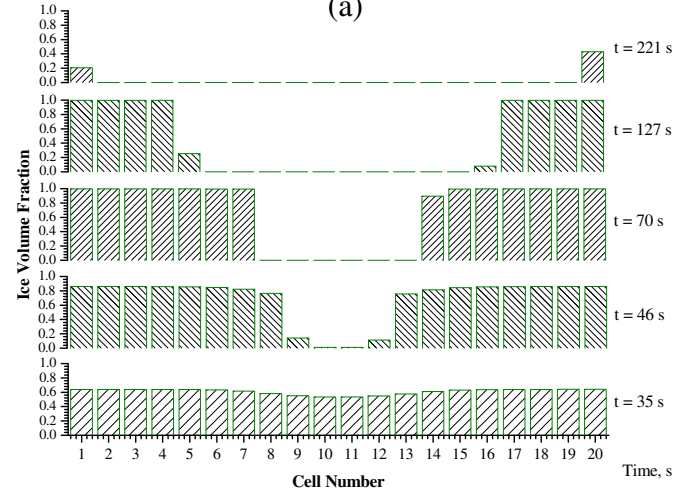


(c)

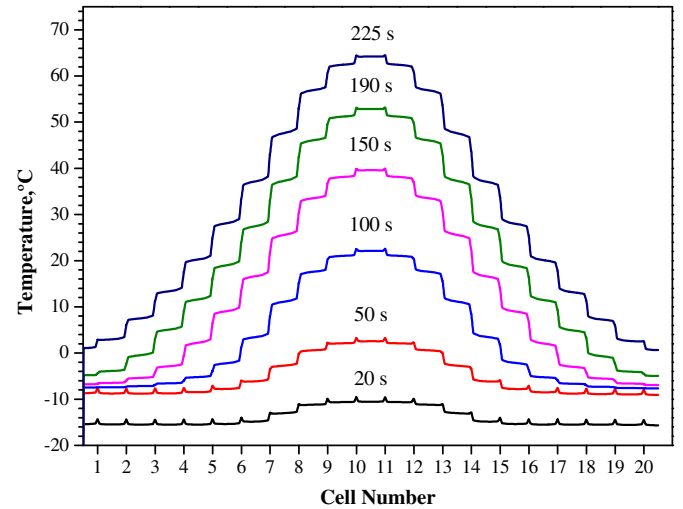
**Fig. 10.** Evolutions of (a) stack voltage and average ice volume fraction in cathode CLs, (b) ice volume fractions in cathode CLs of different cells, and (c) temperature distributions of the 20-cell stack starting from  $-20^{\circ}\text{C}$  at  $0.15\text{ A cm}^{-2}$  with the two end surfaces thermally insulated and with an external heating power of  $100\text{ W}$  (external heating is applied to the individual cell in the middle of the stack).



(a)



(b)



(c)

**Fig. 11.** Evolutions of (a) stack voltage and average ice volume fraction in cathode CLs, (b) ice volume fractions in cathode CLs of different cells, and (c) temperature distributions of the 20-cell stack starting from  $-20^{\circ}\text{C}$  at  $0.15\text{ A cm}^{-2}$  with the two end surfaces thermally insulated and with an external heating power of  $100\text{ W}$  (external heating is applied to the 6 middle cells of the stack).

insignificant. With the VHLC method, the stack voltage first increases due to the membrane hydration, then decreases because some the cells are fully blocked by ice, and finally the dead cells are active again one by one for successful start-up. With proper control of the VHLC method, it is demonstrated that the cold start performance can be improved significantly, which is critically important for PEMFC in automotive applications.

## Acknowledgments

This research is supported by the National Natural Science Foundation of China (Grant No. 51276121), the Natural Science Foundation of Tianjin (China) (Grant No. 12JCYBJC30500), and the Program for New Century Excellent Talents in University.

## References

- [1] E.A. Cho, J.J. Ko, H.Y. Ha, S.A. Hong, K.Y. Lee, T.W. Lim, I.H. Oh, *J. Electrochem. Soc.* 150 (2003) A1667.
- [2] E.A. Cho, J.J. Ko, H.Y. Ha, S.A. Hong, K.Y. Lee, T.W. Lim, I.H. Oh, *J. Electrochem. Soc.* 151 (2004) A661.
- [3] J. Hou, H. Yu, S. Zhang, S. Sun, H. Wang, B. Yi, P. Ming, *J. Power Sources* 162 (2006) 513.
- [4] J. Hou, B. Yi, H. Yu, L. Hao, W. Song, Y. Fu, Z. Shao, *Int. J. Hydrogen Energy* 32 (2007) 4503.
- [5] K. Tajiri, Y. Tabuchi, C.Y. Wang, *J. Electrochem. Soc.* 154 (2007) B147.
- [6] K. Tajiri, Y. Tabuchi, F. Kagami, S. Takahashi, K. Yoshizawa, C.Y. Wang, *J. Power Sources* 165 (2007) 279.
- [7] S. Ge, C.Y. Wang, *Electrochem Solid State Lett.* 9 (2006) A499.
- [8] S. Ge, C.Y. Wang, *Electrochim. Acta* 52 (2007) 4825.
- [9] Y. Ishikawa, T. Morita, K. Nakata, K. Yoshida, M. Shiozawa, *J. Power Sources* 163 (2007) 708.
- [10] M. Cappadonia, J.W. Erning, U. Stimming, *J. Electroanal. Chem.* 376 (1994) 189.
- [11] M. Cappadonia, J.W. Erning, S.M. SaberiNiaki, U. Stimming, *Solid State Ionics* 77 (1995) 65.
- [12] R.C. McDonald, C.K. Mittelsteadt, E.L. Thompson, *Fuel Cells* 4 (2004) 208.
- [13] E.L. Thompson, T.W. Capehart, T.J. Fuller, J. Jorne, *J. Electrochem. Soc.* 153 (2006) A2351.
- [14] E.L. Thompson, J. Jorne, H.A. Gasteiger, *J. Electrochem. Soc.* 154 (2007) B783.
- [15] S. Sun, H. Yu, J. Hou, Z. Shao, B. Yi, P. Ming, Z. Hou, *J. Power Sources* 177 (2008) 137.
- [16] Y. Wang, *J. Electrochem. Soc.* 154 (2007) B1041.
- [17] L. Mao, C.Y. Wang, *J. Electrochem. Soc.* 154 (2007) B139.
- [18] Y. Wang, P.P. Mukherjee, J. Mishler, R. Mukundan, R.L. Borup, *Electrochim. Acta* 55 (2010) 2636.
- [19] M. Sundaresan, R.M. Moore, *J. Power Sources* 145 (2005) 534.
- [20] M. Khandelwal, S. Lee, M.M. Mench, *J. Power Sources* 172 (2007) 816.
- [21] R.K. Ahluwalia, X. Wang, *J. Power Sources* 162 (2006) 502.
- [22] L. Mao, C.Y. Wang, Y. Tabuchi, *J. Electrochem. Soc.* 154 (2007) B341.
- [23] F. Jiang, W. Fang, C.Y. Wang, *Electrochim. Acta* 53 (2007) 610.
- [24] H. Meng, *J. Power Sources* 178 (2008) 141.
- [25] K. Jiao, X. Li, *Electrochim. Acta* 54 (2009) 6876.
- [26] K. Jiao, X. Li, *Int. J. Hydrogen Energy* 34 (2009) 8171.
- [27] Q. Guo, Y. Luo, K. Jiao, *Int. J. Hydrogen Energy* 38 (2013) 1004.
- [28] Y. Luo, Q. Guo, Q. Du, Y. Yin, K. Jiao, *J. Power Sources* 224 (2013) 99.
- [29] K. Jiao, (Ph.D. thesis), University of Waterloo, 2011.
- [30] K. Jiao, I.E. Alaefour, G. Karimi, X. Li, *Int. J. Hydrogen Energy* 36 (2011) 11382.
- [31] K. Jiao, I.E. Alaefour, G. Karimi, X. Li, *Electrochim. Acta* 56 (2011) 2967.
- [32] G. Hu, J. Fan, S. Chen, Y. Liu, K. Cen, *J. Power Sources* 136 (2004) 1.
- [33] K. Jiao, X. Li, *Prog. Energy Combust. Sci.* 37 (2011) 221.
- [34] A.A. Kulikovskiy, *Analytical Modelling of Fuel Cells*, Elsevier, 2010.
- [35] T.E. Springer, T.A. Zawodzinski, S. Gottesfeld, *J. Electrochem. Soc.* 138 (1991) 2334.
- [36] D. Marquardt, *J. Soc. Ind. Appl. Math.* 11 (1963) 431.
- [37] Y. Tabe, M. Saito, K. Fukui, T. Chikahisa, *J. Power Sources* 208 (2012) 366.